PAPER

Check for updates

Asymmetric perinone-based electron-collecting monolayer materials for n–i–p perovskite solar cells†

Julius Petrulevicius, ‡[a] Minh Anh Truong, ‡[b] Maryte Daskeviciene, [a] Giedre Bubniene,[a] Shota Hira,[b] Yasuko Iwasaki, [b] Tadas Malinauskas, [a] Atsushi Wakamiya *[b] and Vytautas Getautis *[a]

A series of asymmetric perinone derivatives (**PERNI**) bearing different substituents (methyl, fluoro, chloro, bromo, and cyano) on the benzimidazole moiety were synthesized and investigated for possible application as electron-collecting monolayer materials in negative–intrinsic–positive perovskite solar cells. These compounds exhibit good thermal stability and suitable frontier molecular orbital energy levels for electron extraction and hole blocking. The perinone-based devices were found to demonstrate comparable power conversion efficiencies and higher operational stability than reference devices using the representative naphthalene diimide-based monolayer material under the same fabrication conditions. Within the **PERNI** series, devices fabricated with the chloro-substituted **PERNI-Cl** were found to tend to exhibit the highest open-circuit voltage and fill factor owing to the smallest energy offset between the lowest unoccupied molecular orbital and the conduction band of the perovskite.

Introduction

Nowadays, energy crises have raised significant concern worldwide, prompting the motivation to develop sustainable energy harvesting technologies. Photovoltaic technologies (PVs) have the potential to play a significant role in the global effort to decarbonize the energy supply by converting renewable solar energy into electricity. Perovskite solar cells (PSCs) are considered to be one of the most promising alternatives to commercial silicon-based solar cell technology. This is due to their skyrocketing power conversion efficiencies (PCEs) and cost-effective fabrication process.[1–4]

Most of the high-efficiency PSCs that have been reported to date are based on a solution-processed layer-by-layer stacking device structure, with a perovskite light-absorber layer sandwiched between the hole-collecting layer (HCL) and the electron-collecting layer (ECL).[5] In the context of solution-processed multi-layered structures, the development of semiconducting materials exhibiting solvent resistance to the

perovskite precursor solution is paramount for the charge-collecting layer situated beneath the perovskite layer (HCL for positive–intrinsic–negative (p–i–n) or ECL for n–i–p PSCs). In this regard, in the case of p–i–n PSCs, chemically adsorbed monolayer materials (or anchorable molecules) have been identified as a suitable replacement for conventional p-type metal oxide- and polymer-based hole-collecting materials (HCMs), including nickel oxide (NiOx), poly(3,4-ethylenedioxythiophene):poly(styrene sulfonate) (PEDOT:PSS), or poly-[bis(4-phenyl)(2,4,6-trimethylphenyl)amine] (PTAA), etc.[6] The molecular structure of monolayer materials generally consists of a π-conjugated core linked with an anchoring group (such as phosphonic acid,[7–10] carboxylic acid,[11–13] boronic acid,[14] silane,[15] etc.) via an alkyl or aryl spacer. The anchoring group can chemisorb onto the surface of transparent conducting oxides (TCOs) to form a robust monolayer that can withstand the subsequent perovskite deposition. Monolayer materials have been shown to exhibit several advantages over conventional materials, including minimal parasitic absorption, low material consumption and facile molecular structure modification.[16–18] Since our initial report in 2018,[7] significant progress has been made in the development of hole-collecting monolayer materials,[19,20] leading to significant progress in p–i–n single-[3,21] and multi-junction[22–27] solar cell devices.

In n–i–p PSCs, n-type metal oxides, such as titanium oxide (TiO$_2$) and tin oxide (SnO$_2$), are the most commonly used

[a] Department of Organic Chemistry, Kaunas University of Technology, Radvilenu pl. 19, Kaunas, 50254, Lithuania. E-mail: vytautas.getautis@ktu.lt
[b] Institute for Chemical Research, Kyoto University, Gokasho, Uji, Kyoto 611-0011, Japan

‡ J. P. and M. A. T. contributed equally to this work.

electron-collecting materials (ECMs). However, together with their intrinsic oxygen vacancy defects,[28] the photo-catalytic activity under ultraviolet light and high-temperature sintering process (>450 °C) of TiO_2[29] and the high batch-to-batch variation of commercial SnO_2 source materials[30] impede their high-throughput production. In light of the accumulated knowledge in p–i–n PSCs, organic monolayer materials are poised to emerge as promising alternatives to these conventional n-type metal oxides. However, despite recent advances in interfacial modifications that have demonstrated significant improvements in charge extraction and device stability,[31] the development of monolayer material-compatible alternatives to metal oxides remains challenging. There are very few reports on electron-collecting monolayer materials for n–i–p PSCs, and these are limited to well-known fullerene,[32–34] naphthalimide,[35,36] and rylene diimide[5,35–38] derivatives. In contrast, there are numerous efforts devoted to developing hole-collecting monolayer materials in p–i–n PSCs.[39]

In our research, we have focused on perinone structure as a potential electron-collecting monolayer material. Perinone (Fig. 1a), the bisbenzimidazole derivative of naphthalenetetra-carboxylic anhydride, is a significant class of dyes and pigments.[40,41] Furthermore, perinone derivatives have the potential to become attractive n-type semiconducting materials for organic electronic devices[42–44] due to their high electron affinity.[45,46] The perinone structure is known for its inherent stability, a desirable trait for ECMs in PSCs that need to withstand operational stresses like heat and prolonged light exposure, contributing to the long-term operational stability of the solar cell. Additionally, perinone derivatives can be chemically modified to fine-tune their frontier molecular orbital energy levels. Thus, achieving an optimal energy level alignment with the perovskite, facilitating efficient electron injection from the perovskite to the ECM, and minimizing energy losses.[41] Most intriguingly, the π-extended version of perinone, perylene

tetracarboxylic acid bisbenzimidazole (Fig. 1a), was used as an n-type semiconductor in the first heterojunction organic solar cell (OSC) developed by Tang in 1986.[47] Nevertheless, perinone derivatives are less developed due to their poor solubility in organic solvents. To the best of our knowledge, there are only two reports using perinone derivatives in the field of PSCs. Song and coworkers developed a series of soluble halogen-substituted perinones (Fig. 1a) by introducing long alkyl[48] or alkoxy phenyl[49] groups into the naphthalene core and used them as perovskite/ECL interfacial materials in p–i–n PSCs, demonstrating promising results in terms of both efficiency and stability.
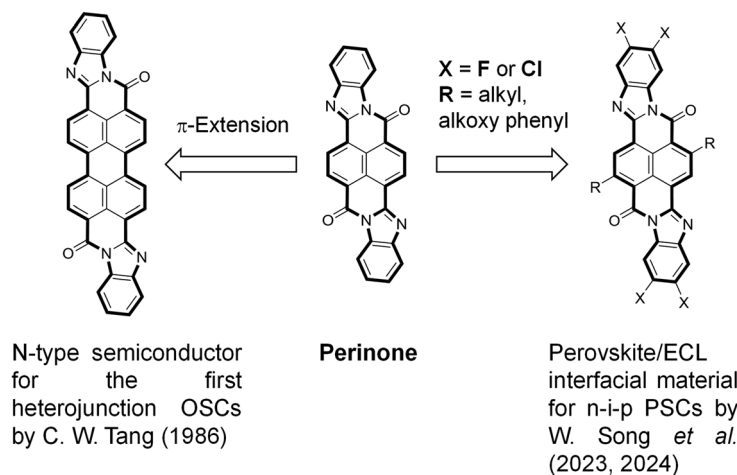
In this study, we sought to address the solubility issue by designing and synthesizing a series of asymmetric perinone molecules (**PERNI**, Fig. 1b) capable of forming monolayers on top of the substrate. In this way, high concentrations of the material in the solution are not required. These molecules contain an imide moiety connected with a methyl phosphonic acid anchoring group on one side and a functionalized benzimidazole moiety on the other (Fig. 1). This approach was taken to mitigate the potential impact of long alkyl (or alkoxy) chains on electron transport, a concern that could hinder the efficacy of the molecules. In addition, we have thoroughly investigated the fundamental properties of these perinone derivatives, encompassing thermal, photophysical and electrochemical characteristics. Finally, we fabricated and evaluated n–i–p PSC devices using these perinone-based monolayers as electron-collecting layers.

Results and discussion

Synthesis

The synthetic route to the perinone derivatives is shown in Scheme 1, and the detailed procedures are provided in ESI.† The phosphonate ester precursor compounds (**1–6**) were

(a) Perinone and Its Derivatives for Photovoltaics:

π-Extension

N-type semiconductor for the first heterojunction OSCs by C. W. Tang (1986)

Perinone

X = F or Cl
R = alkyl, alkoxy phenyl

Perovskite/ECL interfacial material for n-i-p PSCs by W. Song et al. (2023, 2024)

(b) This Work:

PERNI-H (X = H)
PERNI-CH3 (X = CH₃)
PERNI-F (X = F)
PERNI-Cl (X = Cl)
PERNI-Br (X = Br)
PERNI-CN (X = CN)

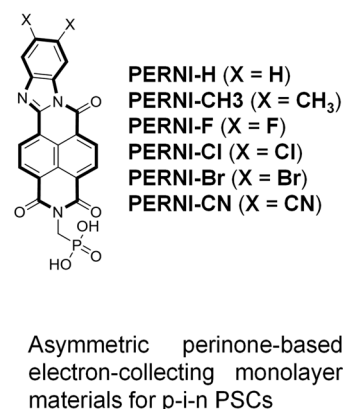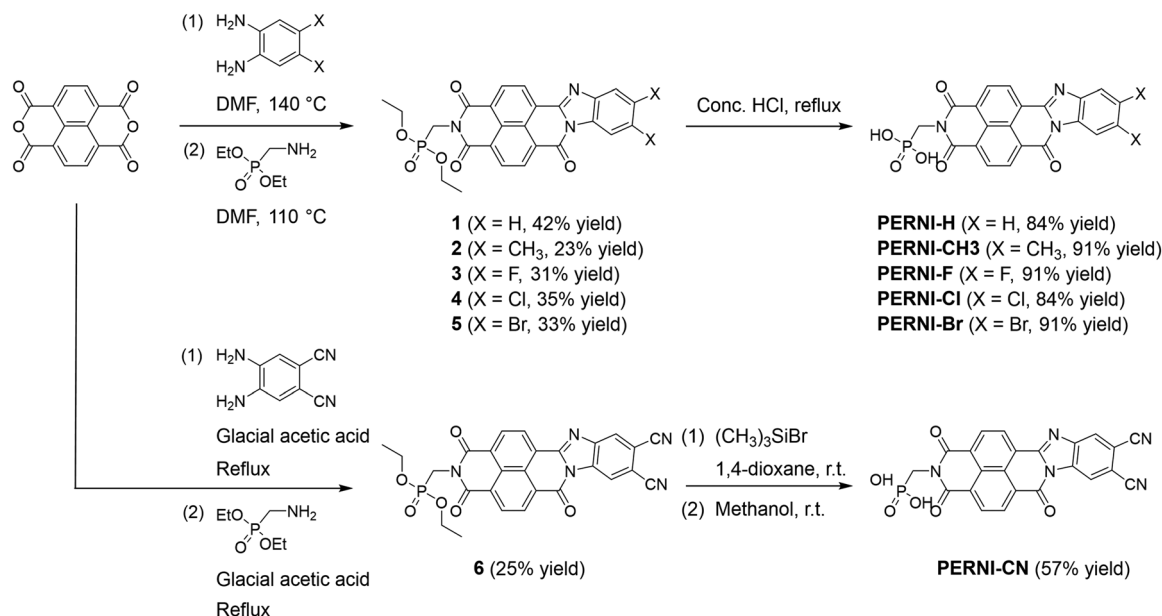Asymmetric perinone-based electron-collecting monolayer materials for p-i-n PSCs

Fig. 1 Chemical structures of (a) perinone, its π-extended derivative, and reported soluble perinone derivatives for p–i–n PSCs, and (b) asymmetric perinone-based anchorable molecules for n–i–p PSCs in this work.

Scheme 1 Synthesis route for asymmetric perinone-based anchorable molecules.

synthesized *via* a one-pot synthesis protocol consisting of a condensation reaction of naphthalene-1,4,5,8-tetracarboxylic dianhydride (1.0 equiv.) and corresponding substituted *o*-phenylenediamine derivatives (1.0 equiv.), followed by the imidation reaction with diethyl(aminomethyl)phosphonate (1.2–1.5 equiv.). The synthesis of compounds **1–5** was carried out in dry dimethylformamide (DMF). However, it was observed that compound **6** undergoes decomposition when DMF is utilized as the reaction solvent. Consequently, for the synthesis of compound **6**, DMF was replaced with glacial acetic acid. The acidic hydrolysis of the phosphonate esters **1–5** with concentrated hydrochloric acid at reflux gave the non-substituted **PERNI-H** (84% yield) and substituted **PERNI** derivatives (91, 91, 84, and 91% yield for **PERNI-CH3**, **PERNI-F**, **PERNI-Cl**, and **PERNI-Br**, respectively). In the case of cyano-substituted **PERNI-CN**, milder hydrolysis conditions were applied using bromo

trimethylsilane at room temperature to prevent any side reactions that may occur at the –CN group. This approach resulted in the isolation of the final product, **PERNI-CN**, with a 57% yield. The chemical structures of the synthesized molecules were verified by means of nuclear magnetic resonance (NMR), elemental analysis, Fourier transformation infrared spectroscopy (FT-IR), and electrospray ionization (ESI) mass spectrometry.

Thermal properties

The thermal stability of the perinone derivatives was evaluated by thermogravimetric analysis (TGA). The measurements were carried out under a nitrogen atmosphere at a scan rate of 10 °C min^{-1}. The results are displayed in Fig. 2 (see also Fig. S1 and Table S1 (ESI†) for phosphonate ester precursor compounds). The temperature corresponding to 5% weight loss (T_{d5}) of the perinone
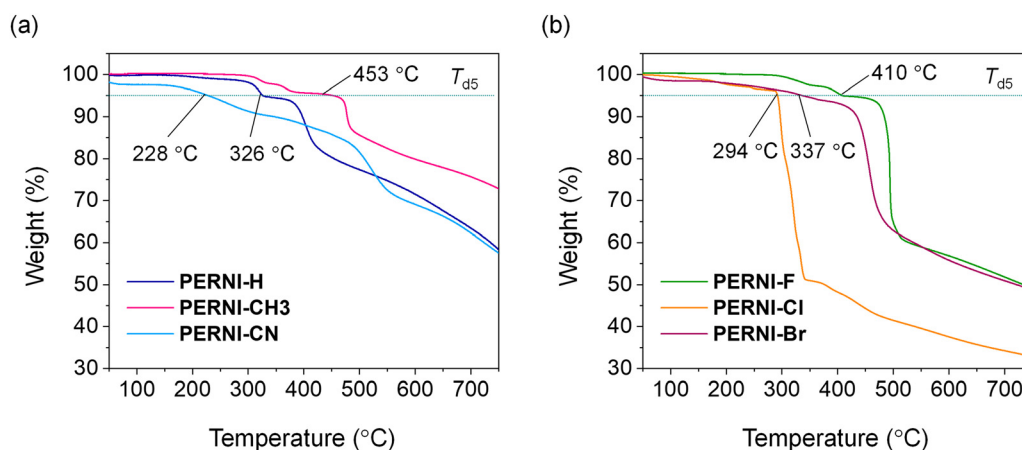

Fig. 2 TGA thermograms of (a) **PERNI-H**, **PERNI-CH3**, and **PERNI-CN**, and (b) **PERNI-F**, **PERNI-Cl**, and **PERNI-Br** at a scan rate of 10 °C min^{-1} under a nitrogen atmosphere.

derivatives was estimated to be in the order of **PERNI-CN** (228 °C) < **PERNI-Cl** (294 °C) < **PERNI-H** (326 °C) < **PERNI-Br** (337 °C) < **PERNI-F** (410 °C) < **PERNI-CH3** (453 °C). The rapid weight loss exhibited by the halogen-substituted perinone derivatives, including **PERNI-F**, **PERNI-Cl**, and **PERNI-Br**, can be ascribed to the release of the halogen atoms. In summary, synthesized perinone derivatives exhibit adequate thermal stability for perovskite solar cell device fabrication by solution process, which is typically conducted at temperatures below 150 °C.

Theoretical calculations

In order to gain insight into the structural and electronic properties of the synthesized perinone molecules, density functional theory (DFT) calculations were performed at the B3LYP/cc-PVDZ level of theory. The side view of DFT-optimized molecular conformations (Fig. 3-bottom) demonstrates that all perinone molecules possess a rigid and planar π-conjugated framework, which is predicted to facilitate intermolecular π–π stacking in the solid state.[50]

As demonstrated in Fig. 3, the highest occupied molecular orbitals (HOMOs) of all molecules are distributed on the entire π-system with the exception of the imide moiety. Conversely, the lowest unoccupied molecular orbitals (LUMOs) exhibit significant delocalization over the perinone fragment. The incorporation of electron-accepting groups such as –F, –Cl, –Br, and –CN, into the benzimidazole moiety results in a
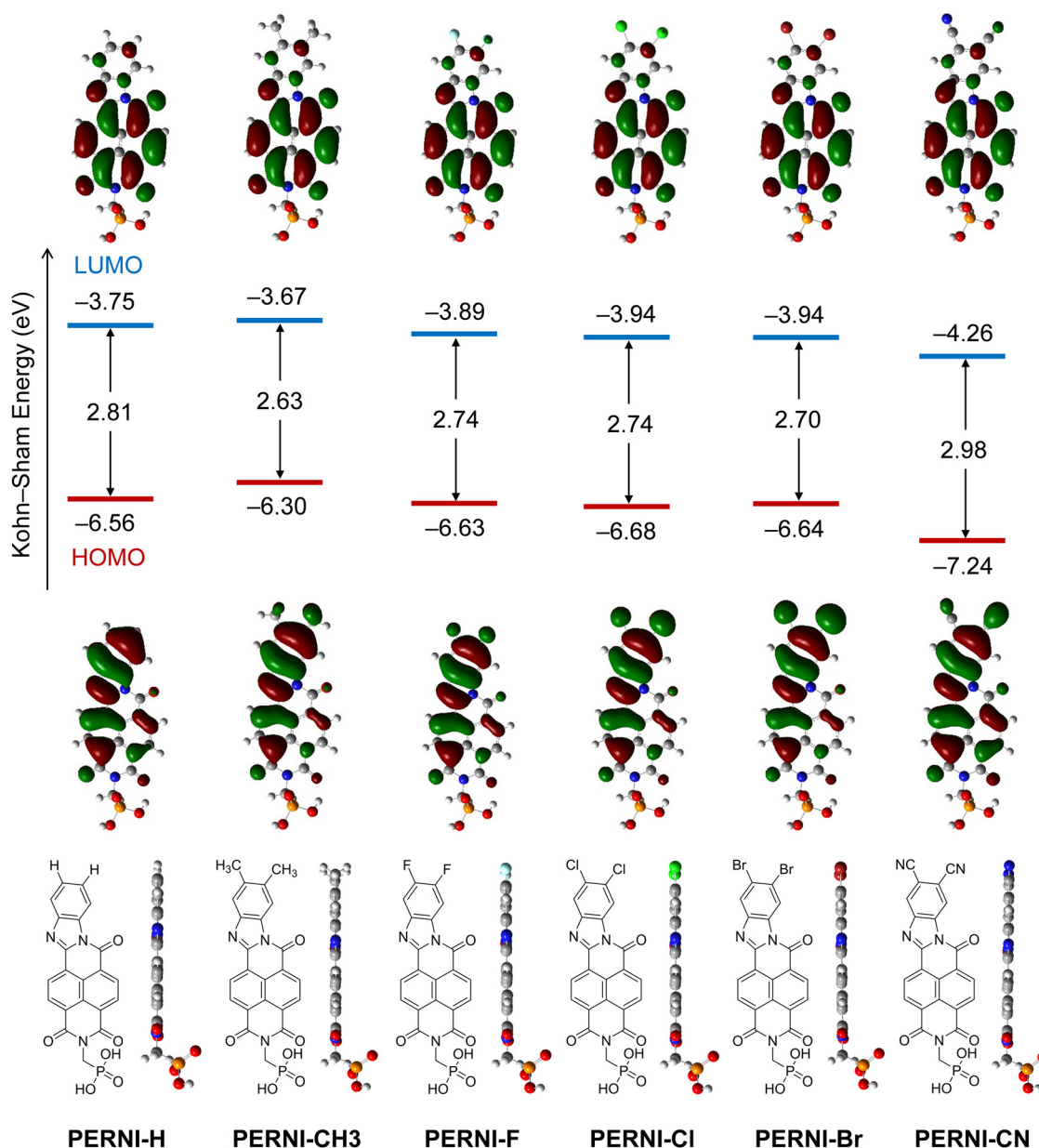

Fig. 3 Frontier Kohn–Sham molecular orbitals and the side view of the optimized molecular conformations for the perinone derivatives obtained from the theoretical calculations at the B3LYP/cc-PVDZ level of theory.

decrease in the energy levels of the frontier molecular orbitals compared to the non-substituted or electron-donating group ($-CH_3$) substituted molecule.

Photophysical properties

In order to investigate the influence of the substituted functional groups on the photophysical properties, the ultraviolet-visible (UV-vis) absorption and photoluminescence (PL) spectra of the perinone derivatives were measured in dimethylacetamide (DMA) solution. The data are presented in Fig. 4 and summarized in Table 1. All compounds exhibit two major absorption bands within the range of 300–325 nanometers (nm) and 400–455 nm, respectively. The broad and intense absorption peak in the longer wavelength region can be attributed to $\pi \rightarrow \pi^*$ transitions. In comparison to non-substituted **PERNI-H** with exhibited a maximum absorption peak (λ_{max}^{Ab}) observed at 433 nm, perinone derivatives with electron-accepting groups demonstrated a hypsochromic shift of 7–20 nm (λ_{max}^{Ab} = 426, 422, 426, and 413 nm for **PERNI-F**, **PERNI-Cl**, **PERNI-Br**, and **PERNI-CN**, respectively). Conversely, a discernible bathochromic shift of 22 nm was evident in the derivative bearing the electron-donating methyl substituent (**PERNI-CH3**, λ_{max}^{Ab} = 455 nm).

A similar trend was obtained for the PL spectra with the peak observed at 626, 675, 604, 533, 590, and 527 nm for **PERNI-H**, **PERNI-CH3**, **PERNI-F**, **PERNI-Cl**, **PERNI-Br**, and **PERNI-CN**, respectively. Consequently, the Stokes shift (λ_{Stokes}) for these perinone derivatives was calculated to be in the range of 111–220 nm. The optical bandgap (E_g) was determined from the intersection (λ_{int}) of the absorption and photoluminescence spectra using the following equation: $E_g = 1240/\lambda_{int}$ (Table 1). The experimental results align with the theoretical calculations, with the smallest and largest optical band gaps observed for **PERNI-CH3** and **PERNI-CN**, respectively.

In comparison to the phosphonate ester precursors **1–6** (Fig. S2 and Table S2, ESI†), the PL spectra of non-substituted **PERNI-H** and methyl-substituted **PERNI-CH3** exhibit a bathochromic shift of approximately 30 nm, while those of **PERNI**

Table 1 Optical properties of the phosphonic acid group containing perinone derivatives

Compound	λ_{max}^{Ab} [a] [nm]	λ_{max}^{Pl} [b] [nm]	λ_{Stokes} [c] [nm]	λ_{int} [d] [nm]	E_g [e] [eV]
PERNI-H	433	626	194	503	2.46
PERNI-CH3	455	675	220	554	2.24
PERNI-F	426	604	178	484	2.56
PERNI-Cl	422	533	111	474	2.62
PERNI-Br	426	590	164	488	2.54
PERNI-CN	413	527	114	458	2.71

[a] Absorption spectra measured in DMA solution 10^{-4} M. [b] Photoluminescence spectra measured in DMA solution 10^{-5} M. [c] Stokes shift $\lambda_{Stokes} = \lambda_{max}^{Pl} - \lambda_{max}^{Ab}$. [d] Intersection point of absorption and emission spectra in DMA solution. [e] Optical band gap was estimated from the intersection of absorption and emission spectra following this equation: $E_g = 1240/\lambda_{int}$.

derivatives with electron-accepting groups, particularly chloro-substituted **PERNI-Cl**, demonstrate a hypsochromic shift up to 58 nm. Freshly prepared and 24 hours-aged DMA solutions of phosphonic acid-containing perinone derivatives (0.1 mM) were exposed to UV radiation (254 nm). As demonstrated in Fig. S3 (ESI†), a discernible alteration in the color of photoemission was observed for **PERNI-F** (from dark yellow to lime), **PERNI-Cl** (from gold to light green), and **PERNI-Br** (from orange to gold). This phenomenon indicates a shift in the emission bands towards shorter wavelengths. This phenomenon can be explained by the formation of H-type aggregates.[51,52] In H-aggregates, the molecular transition dipoles are oriented "face to face". In this configuration, the lower excited state of the two split energy levels generated by dipole interactions is optically forbidden, while the higher one is allowed.

Electrochemical properties

The electrochemical properties of the perinone derivatives were investigated by cyclic voltammetry (CV) measurements in dimethyl sulfoxide (DMSO) solution containing tetrabutylammonium hexafluorophosphate ($^{n}Bu_4N^{+}PF_6^{-}$, 0.1 M) and ferrocene/ferrocenium (Fc/Fc$^+$) as the supporting electrolyte and internal standard, respectively, at a scan rate of 50 mV s^{-1}.
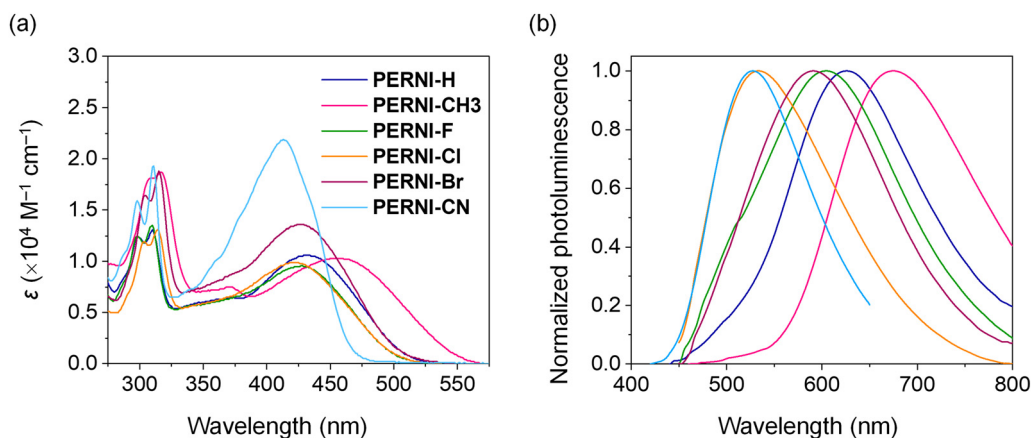

Fig. 4 (a) UV-vis absorption in DMA solution 10^{-4} M and (b) normalized photoluminescence spectra of the phosphonic acid group containing perinone derivatives.

The cyclic voltammograms are shown in Fig. 5, and the electrochemical properties are summarized in Table 2.

The occurrence of quasi-reversible first reduction waves was observed for all compounds. The half-wave reduction potential ($E_{1/2red}$ vs. Fc/Fc$^+$) of **PERNI-H**, **PERNI-CH3**, **PERNI-F**, **PERNI-Cl**, **PERNI-Br**, and **PERNI-CN** was estimated to be -1.01, -0.84, -0.75, -1.10, -0.95, and -0.92 V, respectively. The LUMO energy levels (E_{LUMO}) were calculated to be -4.09, -4.26, -4.35, -4.00, -4.15, and -4.18 eV for **PERNI-H**, **PERNI-CH3**, **PERNI-F**, **PERNI-Cl**, **PERNI-Br**, and **PERNI-CN**, respectively, by using the following equation: $E_{LUMO} = -(5.1 + E_{1/2red\ vs.\ Fc/Fc^+})$, where 5.1 eV is the vacuum energy level of ferrocene.[53–55] Furthermore, the HOMO levels of these perinone derivatives were estimated to be in the range from -6.50 to -6.89 eV. The LUMO and HOMO levels of **PERNI** derivatives are found to be deeper than the conduction bands (CBs) and valence bands (VBs) of typical perovskite materials (CB = -3.90 eV and VB = -5.45 eV for MAPbI$_3$ or CB = -3.99 eV and VB = -5.56 eV for Cs$_{0.05}$FA$_{0.80}$MA$_{0.15}$PbI$_{2.75}$Br$_{0.25}$, MA: methylammonium, FA: formamidinium),[56,57] indicating potential for efficient electron extraction and hole blocking from the perovskite layer.

Fabrication and evaluation of n–i–p perovskite solar cells

The present study aims to evaluate the impact of perinone derivatives as electron-collecting monolayer materials in

Table 2 Electrochemical properties of **PERNI** derivatives obtained from CV and UV-vis measurements

Compound	$E_{1/2red\ vs.\ Fc/Fc^+}{}^a$ [V]	$E_{LUMO}{}^b$ [eV]	$E_{HOMO}{}^c$ [eV]
PERNI-H	-1.01	-4.09	-6.55
PERNI-CH3	-0.84	-4.26	-6.50
PERNI-F	-0.75	-4.35	-6.91
PERNI-Cl	-1.10	-4.00	-6.62
PERNI-Br	-0.95	-4.15	-6.69
PERNI-CN	-0.92	-4.18	-6.89

^{a} Half-wave of reduction potential $E_{1/2red}$ was obtained as an average value between maxima of cathodic and anodic potentials: $E_{1/2red} = 1/2 \times (E_{pc} + E_{pa})$. ^{b} Calculated from the equation $E_{LUMO} = -(5.1 + E_{1/2red\ vs.\ Fc/Fc^+})$,[53–55] where 5.1 eV is the vacuum energy level of ferrocene. ^{c} Calculated from the equation $E_{HOMO} = E_{LUMO} + E_g$, E_g is the optical band gap estimated from UV-vis measurement.

perovskite solar cells. The n–i–p PSCs with a configuration of glass/indium tin oxide (ITO)/electron-collecting layer (ECL)/perovskite/doped 2,2′,7,7′-tetrakis-(N,N-di-4-methoxyphenyl-amino)-9,9′-spirobifluorene (**Spiro-OMeTAD**)/Au (Fig. 6a) were fabricated. For the purpose of comparison, the commercially available naphthalene diimide-based **PANDI** was utilized as the reference for electron-collecting monolayer materials.[37] Additionally, given that the general thickness of conventional metal oxide-based ECL is *ca.* 40 nm,[57] in this study, to mimic a monolayer condition, a very thin layer of SnO$_2$ (*ca.* 3 nm) was also employed as the reference. As previously mentioned, the
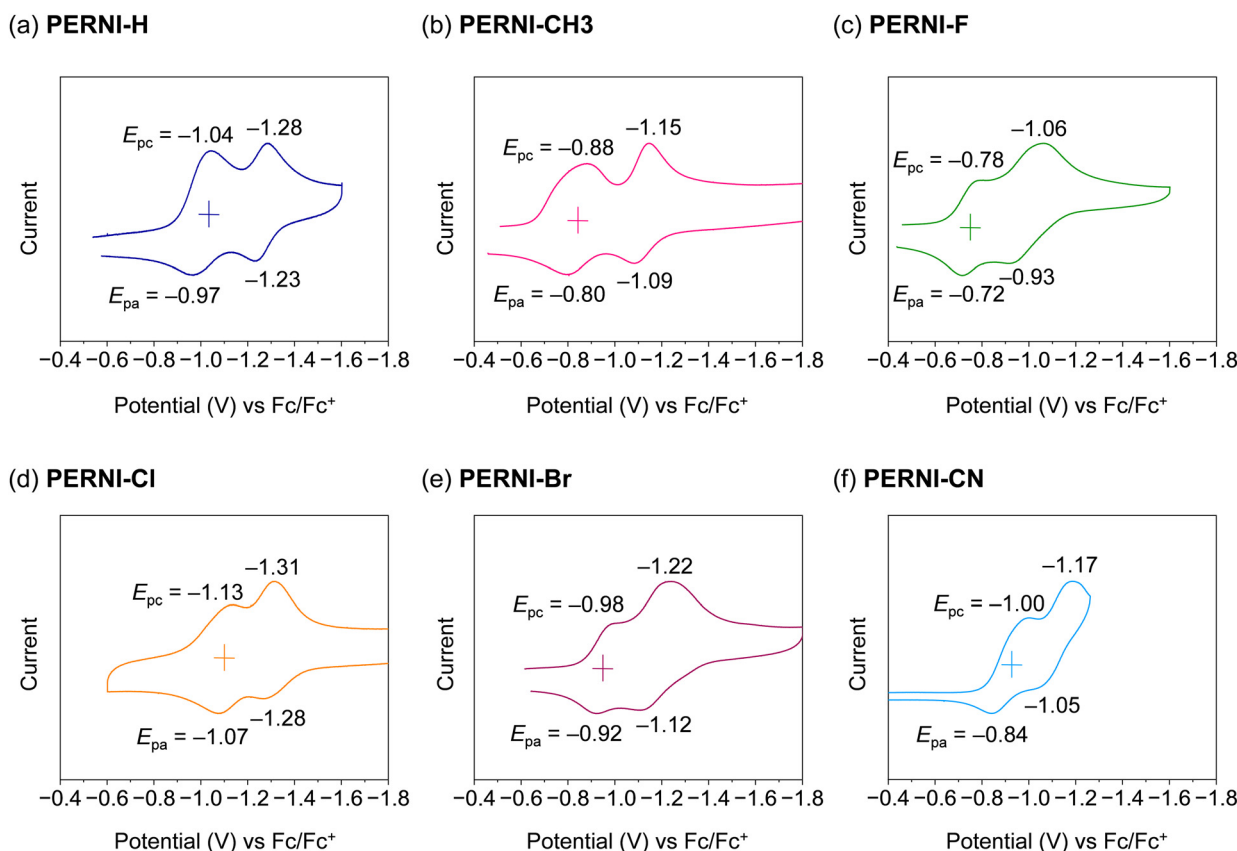

Fig. 5 Cyclic voltammetry curves of **PERNI** derivatives dissolved in DMSO solution at a scan rate of 50 mV s^{-1}.

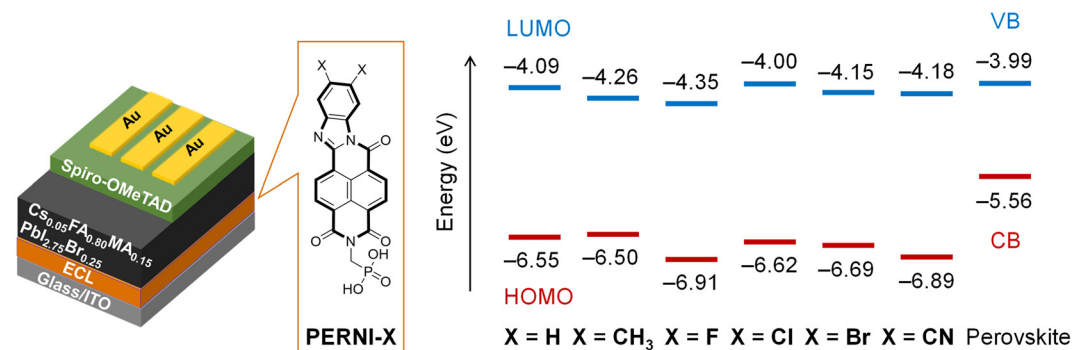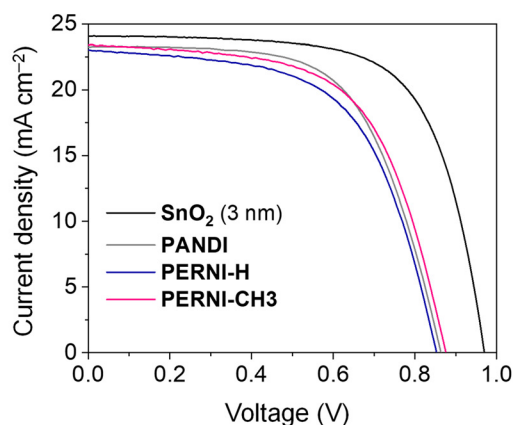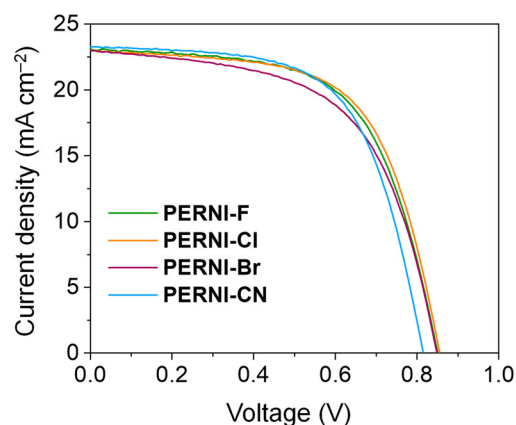## (a) **Schematic Device Structure and Energy Diagram**

(b) *J–V* Curves

(c) *J–V* Curves

Fig. 6 (a) Schematic structure of n–i–p PSC and energy diagram of perinone derivatives and triple-cation mixed halide perovskite used in this work. (b) and (c) *J–V* curves in the reverse scan of the champion devices.

synthesized perinone derivatives exhibit suitable energy level matching (Fig. 6a) with our previously developed triple-cation mixed halide perovskite ($Cs_{0.05}FA_{0.80}MA_{0.15}PbI_{2.75}Br_{0.25}$). For this reason, this perovskite component was selected for this study. The fabrication process for PSC devices is delineated in the ESI.†

The morphology of the perovskite films fabricated on different perinone-based electron-collecting monolayers was evaluated by scanning electron microscopy (SEM). As demonstrated in the top-view (Fig. S4, ESI†) and cross-sectional (Fig. S5, ESI†) SEM images, irrespective of the substituents on the

benzimidazole moiety, all perovskite films exhibit a smooth and pinhole-free surface. The presence of bright grains has been attributed to the presence of excess PbI₂. Notably, the perovskite films fabricated on the **PERNI** derivatives exhibited higher coverage compared to those deposited on **PANDI** (Fig. S6, ESI†). This finding indicates a higher surface wettability of the **PERNI**-based monolayers compared to the **PANDI** counterpart.

The current–voltage (*J–V*) curves for champion devices measured under standard AM 1.5G (100 mW cm⁻²) illumination are shown in Fig. 6b and c. The corresponding device

Table 3 Photovoltaic parameters of n–i–p PSCs with different ECLs derived from *J–V* measurements

ECL	$J_{SC}{}^a$ [mA cm⁻²]	$V_{OC}{}^a$ [V]	FF^a	PCE^a [%]
Thin SnO₂ (3 nm)	24.1 (24.0 ± 0.1)	0.97 (0.97 ± 0.01)	0.67 (0.66 ± 0.01)	15.8 (15.5 ± 0.2)
PANDI	23.3 (22.9 ± 0.6)	0.86 (0.62 ± 0.15)	0.62 (0.53 ± 0.05)	12.5 (7.7 ± 2.8)
PERNI-H	23.1 (21.3 ± 1.4)	0.85 (0.77 ± 0.09)	0.59 (0.47 ± 0.11)	11.7 (8.1 ± 3.1)
PERNI-CH3	23.4 (21.9 ± 1.4)	0.88 (0.81 ± 0.06)	0.61 (0.52 ± 0.09)	12.4 (9.4 ± 2.8)
PERNI-F	23.1 (22.3 ± 0.8)	0.85 (0.81 ± 0.04)	0.61 (0.53 ± 0.08)	12.1 (9.8 ± 2.2)
PERNI-Cl	23.0 (22.6 ± 0.5)	0.86 (0.84 ± 0.02)	0.63 (0.56 ± 0.07)	12.3 (10.6 ± 1.4)
PERNI-Br	23.0 (22.8 ± 0.2)	0.85 (0.83 ± 0.02)	0.58 (0.52 ± 0.06)	11.4 (9.8 ± 1.1)
PERNI-CN	23.3 (23.4 ± 0.7)	0.81 (0.78 ± 0.04)	0.62 (0.61 ± 0.02)	11.8 (11.0 ± 0.5)

^{a} The average and standard deviation values obtained in the reverse scan from 6–18 devices were given in parentheses.

parameters, including short-circuit current (J_{SC}), open-circuit voltage (V_{OC}), fill factor (FF), and PCE, are summarized in Table 3. It is noteworthy that all devices exhibited substantial hysteresis (Table S3 and Fig. S7 and S8, ESI†), particularly in the cases of the PSCs employing electron-collecting monolayers, a finding that aligns with prior reports in the literature.[34–36,58,59] Thus, we used the values derived from the reverse scan to report photovoltaic parameters.

The reference devices employing a 3 nm-thin SnO_2 exhibited a maximum and average PCE of 15.8% and 15.5%, respectively. As no passivation treatment on perovskite films was utilized in the present work, the results can be regarded as comparable to those of previously reported studies.[60] On the other hand, the reference devices fabricated with naphthalene diimide-based monolayer (**PANDI**), which has been reported as one of the most efficient electron-collecting monolayer materials to date,[37] exhibited a lower maximum and average PCE of 12.5 and 7.7%, respectively. This outcome suggests that achieving comparable reproducibility from laboratory to laboratory and even batch to batch is considerably more challenging in the case of electron-collecting monolayer-based n–i–p PSCs compared to p–i–n devices with hole-collecting monolayers. From our perspective, besides intrinsic properties of electron-collecting monolayer materials, such as hydrophobicity and compatible energy levels, the impact of the transparent conducting oxide microstructure[61] is also a crucial factor and should receive more studies.

Getting back to the devices using the perinone derivatives as electron-collecting monolayers. All perinone-based devices exhibited maximum and average PCEs that were comparable to those of devices employing naphthalene diimide-based **PANDI** (see box plots of photovoltaic parameters in Fig. S9, ESI†). The maximum (average) PCE of **PERNI-H**, **PERNI-CH3**, **PERNI-F**, **PERNI-Cl**, **PERNI-Br**, and **PERNI-CN**-based devices was estimated to be 11.7% (8.1%), 12.4% (9.4%), 12.1% (9.8%), 12.3% (10.6%), 11.4% (9.8%), and 11.8% (11.0%), respectively. The enhancement in the average PCE can be attributed to an increase in the average V_{OC} of the perinone-based devices (0.77–0.84 V for perinone derivatives $vs.$ 0.62 V for **PANDI**). Among the devices using the **PERNI** series, those fabricated with chloro-substituted **PERNI-Cl** tend to exhibit the highest V_{OC} and FF, which is correlated with its smallest CB/LUMO energy offset (+0.01 eV for **PERNI-Cl** $vs.$ +0.10 to +0.36 eV for the other **PERNI**). The J_{SC} values derived from the J–V curves of the perinone-based devices are in line with the integrated values estimated from the incident photon-to-current conversion efficiency (IPCE, Fig. S10, ESI†) spectra and comparable to that of the **PANDI**-based reference device.

The present study aims to investigate the influence of electron-collecting layers on the charge separation properties at the ECL/perovskite interface. To this end, steady-state photoluminescence (PL) quenching and time-resolved PL (TRPL) decay for the perovskite films deposited on quartz and different ITO/ECL substrates were measured. As shown in Fig. S11 and Table S4 (ESI†), after the fabrication perovskite layers on ECL substrates, the PL peak intensity was reduced to 48, 32, 14, 13,

12, 12, 11, and 4% for SnO_2, **PANDI**, **PERNI-CH3**, **PERNI-F**, **PERNI-H**, **PERNI-Br**, **PERNI-Cl**, and **PERNI-CN**, respectively, in comparison to the pristine perovskite deposited on a quartz substrate. A double exponential function in which the fast lifetime (τ_1) is associated with the charge transfer quenching at the interface, while the long lifetime (τ_2) is attributed to the charge recombination quenching in the bulk, was used to fit the PL decay. The average TRPL lifetime (τ_{ave}) and τ_2 for the perovskite film fabricated on SnO_2 were found to be 164 and 177 ns, respectively, which are longer than those of the perovskite films deposited on **PANDI** (τ_{ave} = 74 ns, τ_2 = 82 ns) and perinone derivatives (τ_{ave} = 17–63 ns, τ_2 = 21–68 ns). This result correlates well with the trend observed for V_{OC} and indicates that the charge recombination in the perovskite film fabricated on SnO_2 was suppressed compared to those fabricated on **PANDI** or **PERNI** derivatives, leading to higher performance of the SnO_2-based devices.

The operational stability of the devices was evaluated through the implementation of maximum power point tracking (MPPT) measurement in an inert atmosphere at room temperature under AM 1.5G. It is noteworthy that the operational stability of n–i–p devices can be impacted by the incorporation of doped **Spiro-OMeTAD**.[37] To circumvent this concern, for the MPPT measurement, a thin film of **Spiro-OMeTAD** was fabricated by the vacuum deposition method.[56] As shown in Fig. S12 (ESI†), after 100 h, compared to the initial output, the output power of the **PERNI-CN**-, **PERNI-Cl**-, and **PERNI-CH3**-based devices was estimated to be 83, 73, and 60%, respectively, higher than that of the **PANDI**-based reference device (42%). The higher operational stability of the devices fabricated with the **PERNI** derivatives could be attributed to the better coverage and quality of the perovskite films on the **PERNI**-based monolayers compared to the case of **PANDI**.

Overall, as a proof-of-concept, the perinone derivatives (**PERNI** series) were found to be potential electron-collecting monolayer materials in n–i–p PSCs. In this work, a benzimidazole moiety has been modified with various functional groups in order to find the optimal structure. In future work, it would be beneficial to focus on modification of the naphthalene core of these molecules. Thus, finetuning the energy level alignment of the system. Additionally, we observed that the nature of the substituent at benzimidazole moiety has a significant influence on the overall device stability. Therefore, identification of even more compatible functional groups could represent a fruitful avenue for furthering this research.

Conclusions

In summary, a series of asymmetric perinone derivatives bearing different substituents (methyl, fluoro, chloro, bromo, and cyano) on the benzimidazole moiety were synthesized and investigated. These compounds are sufficiently thermally stable. Furthermore, the presence of suitable frontier molecular orbital energy levels suggests their potential to function as electron-collecting materials in n–i–p PSCs. A comparative

analysis was conducted on perinone-based devices and reference devices, utilizing a naphthalene diimide-based monolayer material under identical fabrication conditions. The results indicated that both groups exhibited comparable performance. Among the synthesized perinone derivatives, devices fabricated with the chloro-substituted **PERNI-Cl** were found to exhibit the highest open-circuit voltage and fill factor owing to the smallest energy offset between the lowest unoccupied molecular orbital and the conduction band of the perovskite. The type of substituent at benzimidazole moiety has a marked influence on the overall device stability. We believe that obtained moderate but encouraging results and structure/properties relationships, demonstrated in this work, is another important step towards supplementing or replacing commonly employed metal oxides such as TiO_2, SnO_2, and ZnO as n-type electron transport layers, by adopting electron-collecting molecular monolayers in the n–i–p structure PSCs.

Author contributions

The manuscript was written through contributions of all authors. All authors have given approval to the final version of the manuscript.

Conflicts of interest

A. W. is co-founder and CSO of EneCoat Technologies Co., Ltd.

Data availability

The data supporting this article have been included as part of the ESI.†

References

1 A. Kojima, K. Teshima, Y. Shirai and T. Miyasaka, *J. Am. Chem. Soc.*, 2009, **131**, 6050–6051.

2 G. Szabó, N. G. Park, F. De Angelis and P. V. Kamat, *ACS Energy Lett.*, 2023, **8**, 3829–3831.

3 J. Du, J. Chen, B. Ouyang, A. Sun, C. Tian, R. Zhuang, C. Chen, S. Liu, Q. Chen, Z. Li, X. Wu, J. Cai, Y. Zhao, R. Li, T. Xue, T. Cen, K. Zhao and C.-C. Chen, *Energy Environ. Sci.*, 2025, **18**, 3196–3210.

4 J. Zhou, L. Tan, Y. Liu, H. Li, X. Liu, M. Li, S. Wang, Y. Zhang, C. Jiang, R. Hua, W. Tress, S. Meloni and C. Yi, *Joule*, 2024, **8**, 1691–1706.

5 W. Wang, X. Li, P. Huang, L. Yang, L. Gao, Y. Jiang, J. Hu, Y. Gao, Y. Che, J. Deng, J. Zhang and W. Tang, *Adv. Mater.*, 2024, **36**, 2407349.

6 P. Chen, Y. Xiao, S. Li, X. Jia, D. Luo, W. Zhang, H. J. Snaith, Q. Gong and R. Zhu, *Chem. Rev.*, 2024, **124**, 10623–10700.

7 A. Magomedov, A. Al-Ashouri, E. Kasparavičius, S. Strazdaite, G. Niaura, M. Jošt, T. Malinauskas, S. Albrecht and V. Getautis, *Adv. Energy Mater.*, 2018, **8**, 1801892.

8 M. A. Truong, T. Funasaki, L. Ueberricke, W. Nojo, R. Murdey, T. Yamada, S. Hu, A. Akatsuka, N. Sekiguchi, S. Hira, L. Xie, T. Nakamura, N. Shioya, D. Kan, Y. Tsuji, S. Iikubo, H. Yoshida, Y. Shimakawa, T. Hasegawa, Y. Kanemitsu, T. Suzuki and A. Wakamiya, *J. Am. Chem. Soc.*, 2023, **145**, 7528–7539.

9 A. Al-Ashouri, A. Magomedov, M. Roß, M. Jošt, M. Talaikis, G. Chistiakova, T. Bertram, J. A. Márquez, E. Köhnen, E. Kasparavičius, S. Levcenco, L. Gil-Escrig, C. J. Hages, R. Schlatmann, B. Rech, T. Malinauskas, T. Unold, C. A. Kaufmann, L. Korte, G. Niaura, V. Getautis and S. Albrecht, *Energy Environ. Sci.*, 2019, **12**, 3356–3369.

10 M. A. Truong, L. Ueberricke, T. Funasaki, Y. Adachi, S. Hira, S. Hu, T. Yamada, N. Sekiguchi, T. Nakamura, R. Murdey, S. Iikubo, Y. Kanemitsu and A. Wakamiya, *Angew. Chem., Int. Ed.*, 2024, **63**, e202412939.

11 E. Yalcin, M. Can, C. Rodriguez-Seco, E. Aktas, R. Pudi, W. Cambarau, S. Demic and E. Palomares, *Energy Environ. Sci.*, 2019, **12**, 230–237.

12 M. A. Truong, T. Funasaki, Y. Adachi, S. Hira, T. Tan, A. Akatsuka, T. Yamada, Y. Iwasaki, Y. Matsushige, R. Kaneko, C. Asahara, T. Nakamura, R. Murdey, H. Yoshida, Y. Kanemitsu and A. Wakamiya, *J. Am. Chem. Soc.*, 2025, **147**, 2797–2808.

13 E. Aktas, N. Phung, H. Köbler, D. A. González, M. Méndez, I. Kafedjiska, S. H. Turren-Cruz, R. Wenisch, I. Lauermann, A. Abate and E. Palomares, *Energy Environ. Sci.*, 2021, **14**, 3976–3985.

14 H. Guo, C. Liu, H. Hu, S. Zhang, X. Ji, X.-M. Cao, Z. Ning, W.-H. Zhu, H. Tian and Y. Wu, *Natl. Sci. Rev.*, 2023, **10**, nwad057.

15 H. Tang, Z. Shen, Y. Shen, G. Yan, Y. Wang, Q. Han and L. Han, *Science*, 2024, **383**, 1236–1240.

16 M. Li, M. Liu, F. Qi, F. R. Lin and A. K. Y. Jen, *Chem. Rev.*, 2024, **124**, 2138–2204.

17 Y. Yao, C. Cheng, C. Zhang, H. Hu, K. Wang and S. De Wolf, *Adv. Mater.*, 2022, **34**, 2203794.

18 F. H. Isikgor, S. Zhumagali, L. V. Luis, M. De Bastiani, I. McCulloch and S. De Wolf, *Nat. Rev. Mater.*, 2023, **8**, 89–108.

19 C. E. Puerto Galvis, D. A. González Ruiz, E. Martínez-Ferrero and E. Palomares, *Chem. Sci.*, 2023, **15**, 1534–1556.

20 C. Li, Y. Chen, Z. Zhang, C. Liu, F. Guo, W. Ahmad and P. Gao, *Energy Environ. Sci.*, 2024, **17**, 6157–6203.

21 K. Zhao, Q. Liu, L. Yao, C. Değer, J. Shen, X. Zhang, P. Shi, Y. Tian, Y. Luo, J. Xu, J. Zhou, D. Jin, S. Wang, W. Fan, S. Zhang, S. Chu, X. Wang, L. Tian, R. Liu, L. Zhang, I. Yavuz, H. Wang, H. Yang, R. Wang and J. Xue, *Nature*, 2024, **632**, 301–306.

22 Z. Liu, R. Lin, M. Wei, M. Yin, P. Wu, M. Li, L. Li, Y. Wang, G. Chen, V. Carnevali, L. Agosta, V. Slama, N. Lempesis, Z. Wang, M. Wang, Y. Deng, H. Luo, H. Gao, U. Rothlisberger, S. M. Zakeeruddin, X. Luo, Y. Liu, M. Grätzel and H. Tan, *Nat. Mater.*, 2025, **24**, 252–259.

23 S. Hu, J. Wang, P. Zhao, J. Pascual, J. Wang, F. Rombach, A. Dasgupta, W. Liu, M. A. Truong, H. Zhu, M. Kober-Czerny, J. N. Drysdale, J. A. Smith, Z. Yuan, G. J. W. Aalbers, N. R. M. Schipper, J. Yao, K. Nakano, H. Turren-Cruz, J. M. Ball, D. P. Mcmeekin, K.-A. Zaininger, Z. Liu, N. K. Noel, K. Tajima, W. Chen, M. Ehara, R. A. J. Janssen, A. Wakamiya and H. J. Snaith, *Nature*, 2025, **639**, 93–101.

24 S. Mariotti, E. Köhnen, F. Scheler, K. Sveinbjörnsson, L. Zimmermann, M. Piot, F. Yang, B. Li, J. Warby, A. Musiienko, D. Menzel, F. Lang, S. Keßler, I. Levine, D. Mantione, A. Al-Ashouri, M. S. Härtel, K. Xu, A. Cruz, J. Kurpiers, P. Wagner, H. Köbler, J. Li, A. Magomedov, D. Mecerreyes, E. Unger, A. Abate, M. Stolterfoht, B. Stannowski, R. Schlatmann, L. Korte and S. Albrecht, *Science*, 2023, **381**, 63–69.

25 X. Y. Chin, D. Turkay, J. A. Steele, S. Tabean, S. Eswara, M. Mensi, P. Fiala, C. M. Wolff, A. Paracchino, K. Artuk, D. Jacobs, Q. Guesnay, F. Sahli, G. Andreatta, M. Boccard, Q. Jeangros and C. Ballif, *Science*, 2023, **381**, 59–63.

26 M. Jošt, E. Köhnen, A. Al-Ashouri, T. Bertram, Š. Tomšič, A. Magomedov, E. Kasparavicius, T. Kodalle, B. Lipovšek, V. Getautis, R. Schlatmann, C. A. Kaufmann, S. Albrecht and M. Topič, *ACS Energy Lett.*, 2022, **7**, 1298–1307.

27 X. Jiang, S. Qin, L. Meng, G. He, J. Zhang, Y. Wang, Y. Zhu, T. Zou, Y. Gong, Z. Chen, G. Sun, M. Liu, X. Li, F. Lang and Y. Li, *Nature*, 2024, **635**, 860–866.

28 W. Hui, X. Kang, B. Wang, D. Li, Z. Su, Y. Bao, L. Gu, B. Zhang, X. Gao, L. Song and W. Huang, *Nano Lett.*, 2023, **23**, 2195–2202.

29 N. Fan, Y. Wang, C. Zhang, G. Zhu, G. Du, K. Wei, J. Deng, Z. Luo, L. Yang and J. Zhang, *J. Mater. Chem. A*, 2022, **10**, 8911–8922.

30 J. Deng, X. Huang, Y. Che, X. Wang, X. Zhang, B. Wu, L. Yang and J. Zhang, *Adv. Funct. Mater.*, 2024, **34**, 2408392.

31 K. Li, Y. Zhu, X. Chang, M. Zhou, X. Yu, X. Zhao, T. Wang, Z. Cai, X. Zhu, H. Wang, J. Chen and T. Zhu, *Adv. Energy Mater.*, 2025, **15**, 2404335.

32 Y. C. Wang, X. Li, L. Zhu, X. Liu, W. Zhang and J. Fang, *Adv. Energy Mater.*, 2017, **7**, 1701144.

33 Y. Hou, X. Du, S. Scheiner, D. P. McMeekin, Z. Wang, N. Li, M. S. Killian, H. Chen, M. Richter, I. Levchuk, N. Schrenker, E. Spiecker, T. Stubhan, N. A. Luechinger, A. Hirsch, P. Schmuki, H. P. Steinrück, R. H. Fink, M. Halik, H. J. Snaith and C. J. Brabec, *Science*, 2017, **358**, 1192–1197.

34 P. Topolovsek, F. Lamberti, T. Gatti, A. Cito, J. M. Ball, E. Menna, C. Gadermaier and A. Petrozza, *J. Mater. Chem. A*, 2017, **5**, 11882–11893.

35 L. Li, Y. Wu, E. Li, C. Shen, H. Zhang, X. Xu, G. Wu, M. Cai and W. H. Zhu, *Chem. Commun.*, 2019, **55**, 13239–13242.

36 S. O. Fürer, K. J. Rietwyk, F. Pulvirenti, D. P. McMeekin, M. A. Surmiak, S. R. Raga, W. Mao, X. Lin, Y. Hora, J. Wang, Y. Shi, S. Barlow, D. S. Ginger, S. R. Marder and U. Bach, *ACS Appl. Energy Mater.*, 2023, **6**, 667–677.

37 D. S. Utomo, L. M. Svirskaite, A. Prasetio, V. Malinauskiene, P. Dally, E. Aydin, A. Musiienko, V. Getautis, T. Malinauskas, R. Azmi and S. De Wolf, *ACS Energy Lett.*, 2024, **9**, 1682–1692.

38 F. Ye, D. Zhang, X. Xu, H. Guo, S. Liu, S. Zhang, Y. Wu and W. H. Zhu, *Sol. RRL*, 2021, **5**, 2000736.

39 X. Chen, Z. Yue, H. Yang, B. Xu and Y. Cheng, *Small*, 2025, **21**, 2411312.

40 J. Mizuguchi, *J. Phys. Chem. B*, 2004, **108**, 8926–8930.

41 M. Łapkowski, *Materials*, 2021, **14**, 6880.

42 M. Mamada, C. Pérez-Bolívar and P. Anzenbacher, *Org. Lett.*, 2011, **13**, 4882–4885.

43 M. Mamada, C. Pérez-Bolívar, D. Kumaki, N. A. Esipenko, S. Tokito and P. Anzenbacher, *Chem. – Eur. J.*, 2014, **20**, 11835–11846.

44 R. P. Ortiz, H. Herrera, R. Blanco, H. Huang, A. Facchetti, T. J. Marks, Y. Zheng and J. L. Segura, *J. Am. Chem. Soc.*, 2010, **132**, 8440–8452.

45 E. H. Menke, V. Lami, Y. Vaynzof and M. Mastalerz, *Chem. Commun.*, 2016, **52**, 1048–1051.

46 E. H. Menke, D. Leibold, A. P. Ullrich, Y. Vaynzof and M. Mastalerz, *Org. Chem. Front.*, 2017, **4**, 834–838.

47 C. W. Tang, *Appl. Phys. Lett.*, 1986, **48**, 183–185.

48 X. Zhang, T. Xu, Z. Tian, X. He, S. Zhang, L. Ai, W. Zhang, S. Liu and W. Song, *Chem. Commun.*, 2023, **59**, 5874–5877.

49 S. Zhang, T. Xu, P. Wu, J. Pan, W. Zhang and W. Song, *J. Mater. Chem. C*, 2024, **12**, 4676–4681.

50 T. Okamoto, S. Kumagai, E. Fukuzaki, H. Ishii, G. Watanabe, N. Niitsu, T. Annaka, M. Yamagishi, Y. Tani, H. Sugiura, T. Watanabe, S. Watanabe and J. Takeya, *Sci. Adv.*, 2020, **6**, eaaz0632.

51 N. R. Ávila-Rovelo and A. Ruiz-Carretero, *Org. Mater.*, 2020, **2**, 47–63.

52 S. Ma, S. Du, G. Pan, S. Dai, B. Xu and W. Tian, *Aggregate*, 2021, **2**, e96.

53 C. M. Cardona, W. Li, A. E. Kaifer, D. Stockdale and G. C. Bazan, *Adv. Mater.*, 2011, **23**, 2367–2371.

54 W. Senevirathna, J. Y. Liao, Z. Mao, J. Gu, M. Porter, C. Wang, R. Fernando and G. Sauvé, *J. Mater. Chem. A*, 2015, **3**, 4203–4214.

55 E. Misselwitz, J. Spengler, F. Rominger and M. Kivala, *Chem. Commun.*, 2025, **61**, 5754–5757.

56 M. A. Truong, H. Lee, A. Shimazaki, R. Mishima, M. Hino, K. Yamamoto, K. Otsuka, T. Handa, Y. Kanemitsu,

R. Murdey and A. Wakamiya, *ACS Appl. Energy Mater.*, 2021, **4**, 1484–1495.

57 S. Daskeviciute-Geguziene, M. A. Truong, K. Rakstys, M. Daskeviciene, R. Hashimoto, R. Murdey, T. Yamada, Y. Kanemitsu, V. Jankauskas, A. Wakamiya and V. Getautis, *ACS Appl. Mater. Interfaces*, 2024, **16**, 1206–1216.

58 Y. Miyake, T. Nakamura, M. A. Truong, R. Murdey and A. Wakamiya, *Chem. - Asian J.*, 2025, **20**, e202401344.

59 K. Wojciechowski, S. D. Stranks, A. Abate, G. Sadoughi, A. Sadhanala, N. Kopidakis, G. Rumbles, C. Z. Li, R. H. Friend, A. K.-Y. Jen and H. J. Snaith, *ACS Nano*, 2014, **8**, 12701–12709.

60 W. S. Suh, G. H. Park, S. H. Jung, Y. N. Lee, H. S. Kim, J. H. Pan and W. I. Lee, *Sustainable Energy Fuels*, 2024, **8**, 5214–5224.

61 S. Kralj, P. Dally, P. Bampoulis, B. Vishal, S. De Wolf and M. Morales-Masis, *ACS Mater. Lett.*, 2024, **6**, 366–374.